Following the phase transitions of iron in 3D with X-ray tomography and diffraction under extreme conditions

Eglantine Boulard, Christophe Denoual, Agnès Dewaele, Andrew King, Yann Le Godec, Nicolas Guignot

Journal Pre-proof

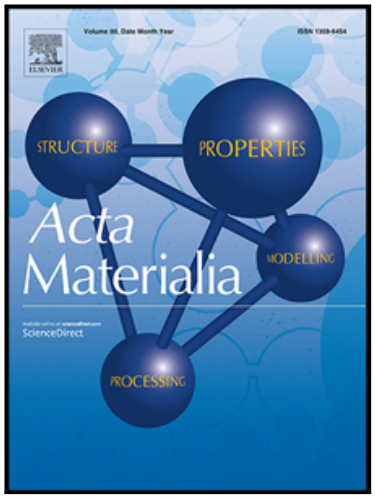

Following the phase transitions of iron in 3D with X-ray tomography and diffraction under extreme conditions

Eglantine Boulard, Christophe Denoual, Agnès Dewaele, Andrew King, Yann Le Godec, Nicolas Guignot

PII: S1359-6454(20)30287-1
DOI: https://doi.org/10.1016/j.actamat.2020.04.030
Reference: AM 15977

To appear in: *Acta Materialia*

Received date: 7 February 2020
Revised date: 9 April 2020
Accepted date: 12 April 2020

Please cite this article as: Eglantine Boulard, Christophe Denoual, Agnès Dewaele, Andrew King, Yann Le Godec, Nicolas Guignot, Following the phase transitions of iron in 3D with X-ray tomography and diffraction under extreme conditions, *Acta Materialia* (2020), doi: https://doi.org/10.1016/j.actamat.2020.04.030

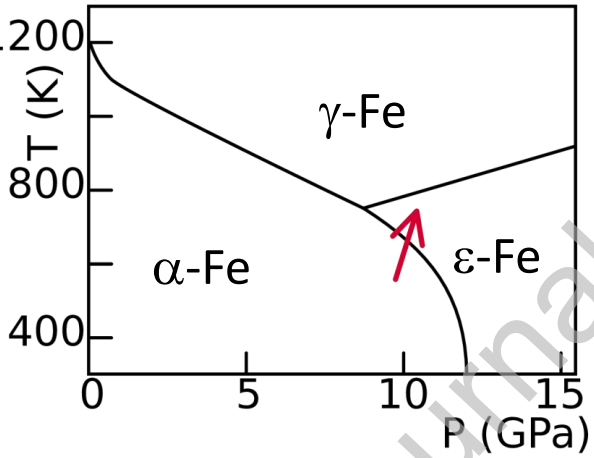

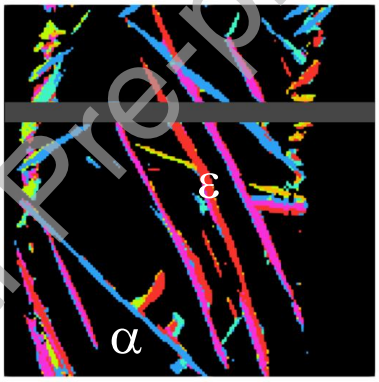

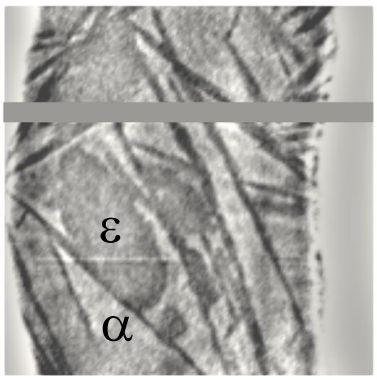

Following the phase transitions of iron in 3D with X-ray tomography and diffraction under extreme conditions

Eglantine Boulard[a], Christophe Denoual[b], Agnès Dewaele[b], Andrew King[c], Yann Le Godec[a], Nicolas Guignot[c]

[a]*Sorbonne Université, Muséum National d'Histoire Naturelle, UMR CNRS 7590, IRD, Institut de Minéralogie, Physique des Matériaux et Cosmochimie - IMPMC, 4 Place Jussieu, 75005 Paris, France*
[b]*CEA, DAM, DIF, F-91297 Arpajon, France*
[c]*Synchrotron Soleil, F-91192 Saint Aubin, France*

Abstract

Transformations of iron at high pressure and temperature has significant implications in Fe-based materials technology as well as in planetary science due to its prominent presence in terrestrial planet cores. However, a detailed understanding of processes involved in the high temperature α-Fe $\leftrightarrow$ γ-Fe and the high pressure α-Fe $\leftrightarrow$ ϵ-Fe transformations is still lacking. In this study, we monitored *in situ* the orientations and mobility of the interfaces of coexistence of parent and daughter phases of iron upon transitions around the α-γ-ϵ triple point. We show that in α-Fe $\leftrightarrow$ ϵ-Fe transitions, a displacive mechanism induces typical martensitic microstructures, but is followed by a second likely reconstructive step which transforms most of the sample. Under similar pressure, temperature and heating rate conditions, α-Fe $\leftrightarrow$ γ-Fe transformations appear to be purely reconstructive. This work provides for the first time a complete 3D microstructural *in situ* characterization of iron structural transitions under extreme conditions that clarifies their fundamental mechanisms.

1. Introduction

The phase diagram of iron is complex in the 0-20 GPa range due to the existence of several crystalline phases [1]. Their relative stability is subject to an interplay between electronic correlations, magnetism, and lattice vibrations and has fundamental bearing in geophysics as iron is the most abundant element in planetary cores, and technological applications particularly for steel industry.

Under ambient conditions, iron is ferromagnetic and adopts a cubic (bcc) α-Fe structure. When it is heated at ambient pressure, α-Fe loses long-range magnetic order above the Curie point at 1043K and transforms into

an fcc paramagnetic γ-Fe phase at 1188 K via a soft mode [2, 3]. This transition is fundamental for metallurgy as most heat treatments of steels are based on its existence: many hardened steels have a peculiar microstructure, called martensitic, formed during $\gamma \rightarrow \alpha$ transformation via quenching. This microstructure exhibits individual grains of the daughter phase, with characteristic shapes (lenticular plates, wedges, etc.) and relative orientations. Allotropic transformations which give rise to a martensitic microstructure (also termed martensitic) are displacive transformations in the sense that the atoms of the parent phase move cooperatively by less than one interatomic distance to form the daughter phase [4]. The orientations of crystals in the two phases are then related by so-called orientation relations (OR). The shape change of the crystal caused by the transformation creates stresses released by plastic strain: associated defects are thus observed after displacive transformations (dislocations, twins, stacking faults). A displacive mechanism differs from a reconstructive mechanism, which involves atomic diffusion to form the daughter phase. Surprisingly, studies of $\alpha \leftrightarrow \gamma$ transformation mechanisms in pure iron are scarce [5, 3, 6, 7] and their exact nature remains debated.

Compressed at ambient temperature, α-Fe transforms into hexagonal closed packed (hcp) ϵ-Fe around 13 GPa. The discovery of ϵ-Fe is one of the most important of high-pressure science, made some 60 years ago with shock-wave compression technique [8], and confirmed by static compression coupled with X-ray diffraction to determine its structure [9, 10]. The driving force of the transformation at the atomic scale, linked to the loss of ferromagnetic order [11], is captured by density-functional theory [12], although its exact mechanism is not yet understood [13]. ϵ-Fe has a wide stability range in pressure and temperature and is the likely major phase of the Earth's inner core, above 330 GPa and 6000 K [14]. The martensitic character of the α-Fe $\leftrightarrow$ ϵ-Fe transformations is witnessed by the hysteresis between the direct and reverse transitions [15, 16]. This view has been strengthened by recent *in situ* measurements of orientation relations between α and ϵ phases, typical of one martensitic path, the Burgers path [17], under static [18, 19] or dynamic [20, 21] compression. Microstructural studies have been performed only *ex situ* on decompressed samples [22, 23]. However, interpretation of microstructures after two transformations ($\alpha \rightarrow \epsilon \rightarrow \alpha$) is nontrivial [24]. A detailed understanding of the micro and meso-scale mechanism (exact displacive/reconstructive character, nucleation, propagation and associated plasticity mechanisms) is lacking. The morphological features (grains shape, boundaries, orientations) or microstructure - needed for this understanding are usually provided by EBSD on polished surfaces [25] or diffraction contrast tomography in bulk [26], but these measurements have not been performed

in bulk samples under extreme conditions.

To tackle this challenge, we propose a new experimental approach to characterize, *in situ* and in 3D, the microstructure induced by the transitions around α-γ-ϵ triple point in pure iron ($\sim$8.7 GPa, 750 K [27]). As phase transitions were induced by compressing/heating of single crystals in a Paris-Edinburgh press, we probed the orientations and mobility of the coexistence interfaces between parent and daughter crystalline phases by coupling propagation based X-ray phase contrast tomography and X-ray diffraction (XRD). The experimental data have been interpreted with a kinematic compatibility model, which sharply constrains the transition mechanisms.

2. Experimental details

Single crystal samples of α-Fe oriented with a vertical cubic axis, have been compressed and heated, up to $\sim$11 GPa and $\sim$1000 K, in Paris-Edinburgh presses with different designs as detailed below. A total of 14 runs have been performed. Tomography and XRD have been collected almost simultaneously - within minutes - under high pressure and temperature. Thanks to the joined use of homogeneous single crystals as starting samples and X-ray phase contrast imagining, minor differences in densities between the crystalline phases formed under extreme conditions (as low as $\sim$2%) could be resolved and the surface of coexistence imaged. Orientation relations between these phases have been determined with XRD.

2.1. Starting materials and experimental setup

Starting material consisted of single crystal irons, purity 99.994+%, shaped in cylinders with axis in [100] direction purchased from Mateck GmbH, Germany. Iron single crystals were loaded into Paris-Edinburgh (PE) Press assembly with BN capsule, graphite furnace and amorphous boron epoxy or pyrophyllite gasket. We used three sizes of single crystal iron: 2 x 2 mm (diameter, length), 1.2-1.5 x 1.5 mm and 0.8 x 1.5 mm loaded into gaskets of size 10-3.5 mm, 7-2.4 mm and 5-1.5 mm, respectively, to cover a large range of pressure conditions up to $\sim$11 GPa -1100 K. A sketch of the sample assembly is represented in Fig. 1b. High pressure and temperature experiments were performed in large volume PE presses with either tungsten carbide anvils (for 10 and 7 mm gasket sizes) or sintered diamond anvils (for the 5 mm gasket size). Three kind of PE presses have been used: a classic 4 columns PE press [28], a modified compact 2 columns VX9 PE press [29] recently developed for *in situ* tomography called "UtoPEC" [30] and a Rotational anvil PE press (RotoPEC) [31].

The sample assembly is designed so that the uniaxial stress imposed by the press is partially transformed into a hydrostatic pressure thanks to the

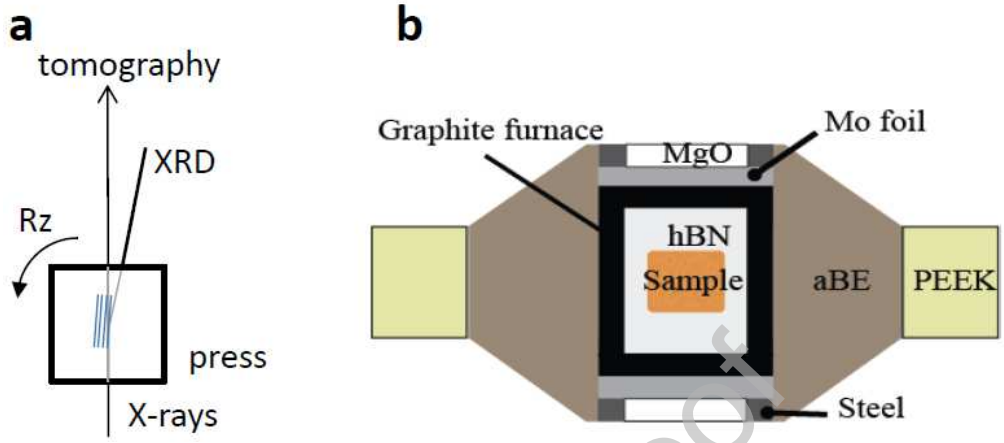

Figure 1: **Experimental setup** a. Sketch of the coupled X-ray diffraction (XRD) and tomography setup. During exposure, the Paris-Edinburgh press is rotated around a vertical axis by an angle Rz=0-180° b. Schematic illustration of the cell assembly used for the experiments. The sample diameter varies between 2mm and 0.8mm, depending on the goal pressure. aBE: amorphous Boron Epoxy; PEEK: polyetheretherketone

shape of the boron-epoxy/pyrophillite gasket and the use of a soft h-BN pressure transmitting medium. However, all samples have been plastically strained as attested by their dimensions measured after unloading, with a decrease of their height by 10 to 25%. In order to diminish the non-hydrostatic stress on the sample, the temperature was first increased at about 400-500 K before compression to its target pressure. Note that an increase in temperature intrinsically increases the pressure on the sample. Temperature (pressure) was changed with approximate rates of 10^2 K/s (10^{-3} GPa/s).

Experiments were conducted on the high pressure beamline PSICHE at Synchrotron Soleil [32] (see Fig. 1a). We analyzed simultaneously (within a few minutes) the sample by X-ray propagation based phase contrast imaging and energy dispersive diffraction through the PE press at high pressure and temperature. Phase contrast tomography is an X-ray imaging technique in which the perturbation of the phase of the X-ray wavefront is used as a contrast mechanism, capable of reveal minor variations in density.

2.2. Tomography measurements

X-ray imaging were performed by the use of a pink beam with a mean energy around 65 KeV or 71.9 keV (see supplementary Figure 1). A visible-light image was formed using a 50, 90 or 250 μm-thick LuAG scintillator screen and transmitted to the Hamamatsu ORCA Flash4.0 sCMOS camera using a 10, 5 or 2.5x microscope objective depending on the sample size. This gives an effective pixel size of 0.63, 1.3 and 2.26 microns, respectively. While

the 4 columns on a classic PE press produce artefacts in the volume reconstructions and about 45° of missing data in two 22.5° wedges, the RoToPEC has no columns shadow, and the UtoPEC has a very small shadow on the X-ray tomograms (the blind angle being 15°). Typical UtoPEC or classic PE press tomographic dataset consisted of 700 projections with typical exposure times of 30 ms for each image. Thus, each tomogram has a collection time of about 20 s [30]. In addition, reference images were recorded before and after the projections and a complete dataset is recorded in 1 min 30s. The possibility to perform high-speed tomography was important for the current experiments, as the measured system can evolve with typical times of the order of a few minutes. However, due to the rotation speed of the RoToPEC's anvils, collection of a tomogram with the RoToPEC is ∼20 min. Reconstructions sections of the sample were performed using a single iteration correction implemented using PyHST2 [33], employing Paganin phase retrieval to minimize ring artefacts. A first reconstruction is performed, which is segmented, and then forward projected to create ideal projections. The difference between the real and the ideal projections is used to determine a correction that will be applied to the projections before the final reconstruction.

2.3. X-ray diffraction measurements

Energy dispersive X-ray diffraction (XRD) patterns were collected with a CAESAR detector [34] placed at a fixed angle of 8°. This angle has been precisely calibrated using an Au reference sample. The volume scanned with XRD was limited by the use of two sets of slits to a rhombus of 50 to 100 microns width, 500 to 1000 microns depth and 100 to 200 microns height.

Because the starting samples were single crystals, XRD patterns of the sample were collected upon rotation of the press by Rz angle with the geometry presented in Fig. 1. Each XRD spectrum was collected upon 5° of rotation; in total, 36 spectra were collected from Rz=0° to Rz=180° (20 minutes collection time). Different vertical crystal planes can enter in diffraction conditions at different Rz angles. This allowed measuring the orientation of the starting single crystal (see Supplementary Fig. 2), but not to fully orient any crystal formed in the course of the experiment because the XRD is collected only in a horizontal plane.

The temperature was determined by previous power-temperature calibrations using thermocouples as well as from observation of the α-γ phase transition: a linear input power temperature relationship was assumed. The pressure was determined using Fe and hBN unit cell volumes and their respective thermal equation of states [35, 36, 37]. The unit cell volumes have been calculated using $\{200\}_{\mathrm{bcc}}$, $\{200\}_{\mathrm{fcc}}$, $\{0002\}_{\mathrm{hcp}}$ and $\{1\bar{1}01\}_{\mathrm{hcp}}$ XRD peaks. The *P-T* paths followed in several runs are presented in Fig. 2; corresponding data are listed in Tables C.1, C.2 and C.3.

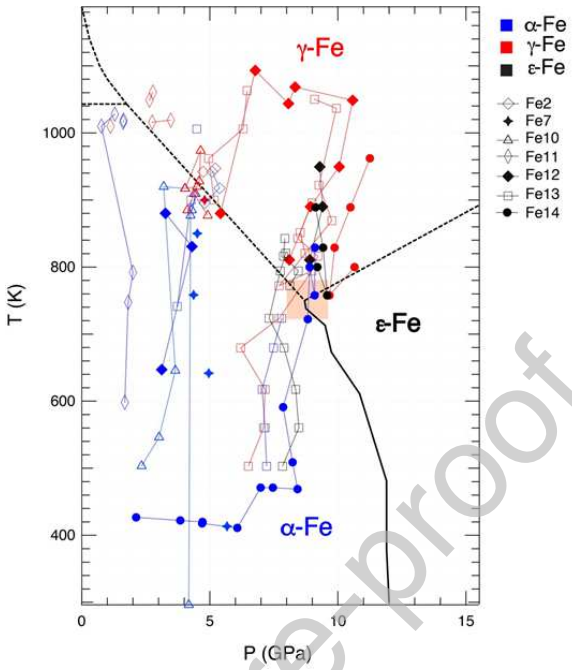

Figure 2: *P-T* **paths followed in selected experiments.** The phase boundary lines are from Ref. [27].

3. Results

3.1. Transformations α to γ and γ to α

The $\alpha \rightarrow \gamma$ transformation has been induced by temperature increase in different runs between 1 GPa (Fig. 3) and 6 GPa, producing similar microstructures. α-Fe single crystals were heated up to ∼450 K, subsequently compressed to the target pressure, and then further heated up to synthesize the γ-Fe phase. The γ phase appears on the hottest outer part of the starting α-Fe single crystal sample, and progressively grows at the expense of the α phase when the temperature is increased. The single and smooth α-γ interface roughly follows one isotherm within the sample; although it can be locally planar (Fig. 3 and Supplementary Fig. 3).

Starting from one crystal oriented with one vertical cubic axis, a few to several γ-Fe orientations are produced by the phase transition in the volume scanned by XRD (Supplementary Fig. 4). Here, XRD is collected within one horizontal plane and does not allow us to fully determine the orientation of any single crystal formed. Nevertheless, if one assumes that the transition mechanism is martensitic, γ-Fe XRD peaks orientations can be computed using expected orientation relations (OR): in iron alloys, the Kurdjumov-Sachs OR are dominant [4, 23, 5]. Here, the γ-Fe XRD peaks expected with

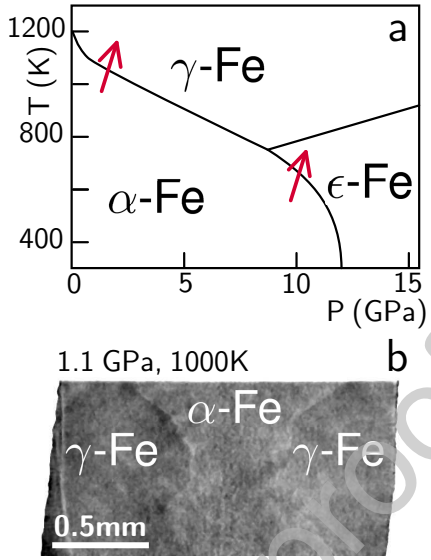

Figure 3: **a. Phase diagram of iron** after Ref. [27]. P-T paths corresponding to tomographies in **b** and Fig. 5 are indicated by red arrows. **b.** $\alpha \rightarrow \gamma$ **transformation.** Vertical slice of a tomographic reconstruction collected around 1.1 GPa and 1000 K. The phase in dark gray (i.e. the densest) is the γ-Fe (2.3% density difference with α-Fe [27]). Other vertical slices exhibit a similar α-γ interface, which approximately follows one isotherm. The starting sample was a single crystal of α-Fe oriented with one vertical cubic axis.

this OR were observed only in some cases.

The γ to α transformation has been induced by temperature decrease, producing a similar interface. The starting single crystal orientation was partially recovered after one α to γ to α cycle, evidencing a memory behaviour of the system.

3.2. Transformation α to ϵ and ϵ to α.

In one run, a single crystal of α-Fe was compressed to about 10 GPa at 400-470 K, and the α-ϵ transformation was induced by heating to $\sim$800 K around this pressure. The first tomographic reconstruction collected after phase transformation onset (Fig. 4) shows numerous transformed platelets of up to 30 microns thick, with a higher density close to the surfaces. Large platelets extend on the whole sample volume (purple arrows in Fig. 4d), while smaller ones are limited by these large platelets and form a typical martensitic microstructure (blue arrows in Fig. 4f). We will discuss later whether the surfaces of these platelets can be identified as *habit planes*, the planar interfaces between parent and daughter phases observed in displacive transformations. The tomographic reconstruction also shows ϵ-Fe solid grains, sometimes wedge-shaped, with planar or curved α-ϵ interfaces (red arrows in Fig. 4d) .

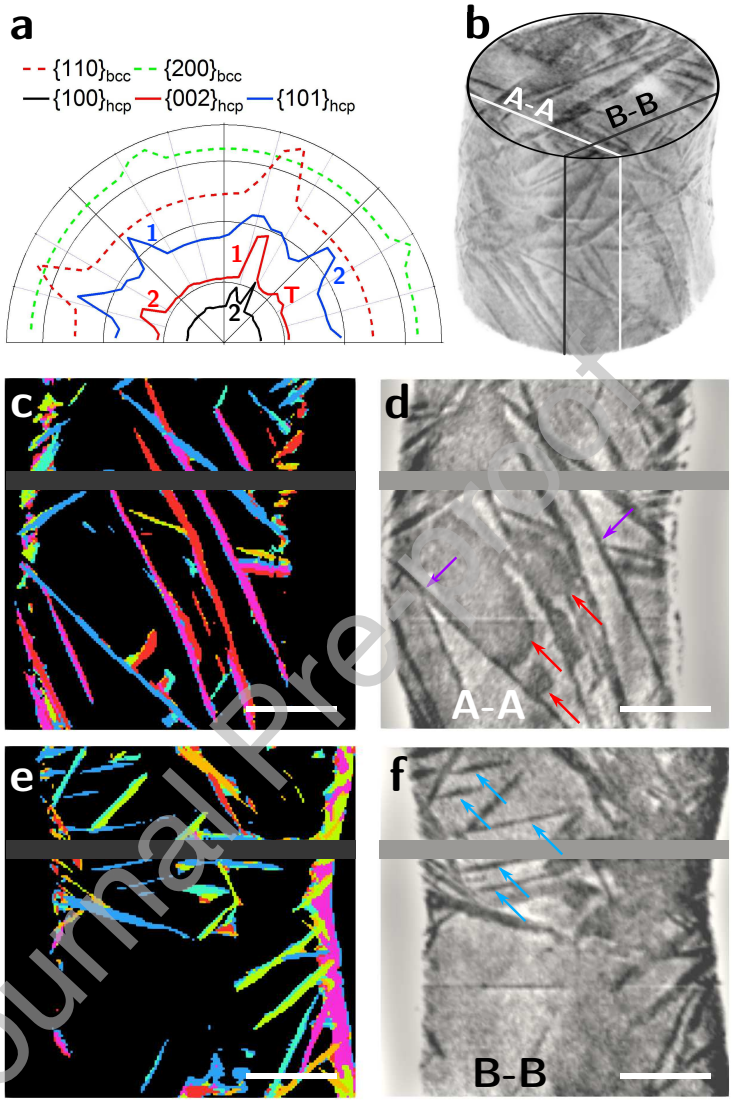

Figure 4: **Microstructure induced by $\alpha \rightarrow \epsilon$ transformation in iron. a,** measured with X-ray diffraction (XRD): XRD peaks intensity is represented vs sample Rz rotation (see Fig. 1). Each color corresponds to a lattice plane family. α-Fe peaks correspond to one orientation of a bcc crystal, with one vertical cubic axis. ϵ-Fe peaks correspond to the orientations expected for the variants of Burgers path (in particular, variants 1 and 2 with basal $\{0002\}_{\text{hcp}}$ plane parallel to one $\{110\}_{\text{bcc}}$ plane seen on the XRD record), except the peak labelled T which can be predicted by $\left\{01\bar{1}2\right\}\left\langle 0\bar{1}11\right\rangle$ twinning of one variant. **b,** View of the tomographic reconstruction collected at 10.6 GPa and 800 K. Dark (light) zones correspond to ϵ-Fe (α-Fe). A-A and B-B indicate the section planes for **c, d** and **e, f**, respectively. **c, e,** A-A and B-B section planes. The colouring of platelets corresponds to the variants identified from their surface orientations (scale in Fig. 7). **d, f,** A-A and B-B section planes as seen in the tomographic reconstruction. The horizontal gray line is masking a reconstruction artefact. The purple and blue arrows point to platelets formed during the first stage of the $\alpha \rightarrow \epsilon$ transformation, while red arrows point to a second stage transformed zones. The scale bar corresponds to 0.2 mm.

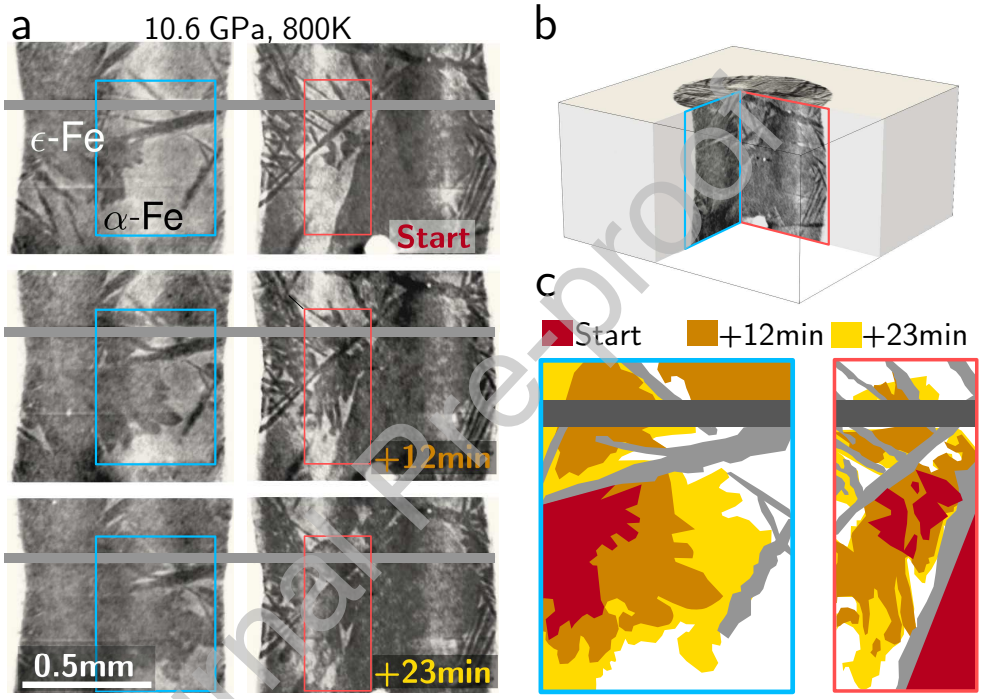

Figure 5: **a.** $\alpha \rightarrow \epsilon$ **transformation monitored with tomography.** Two (left, right) tomographic slices collected at different times around 10.6 GPa and 800 K. The phase in dark gray (i.e. the densest) is the ϵ-Fe (3.5% density difference with α-Fe). The blue and red boxes show the regions where the progress of $\alpha \rightarrow \epsilon$ transformation has been analyzed as represented in **c.** The starting sample was a single crystal of α-Fe oriented with one vertical cubic axis. **b.** 3D tomographic reconstruction: the two slices represented in **a.** are indicated. **c.** Progress of $\alpha \rightarrow \epsilon$ transformation. The grey regions indicate the ϵ-Fe platelets formed in the first stage (see text). The red to yellow regions indicate the granular ϵ-Fe crystals formed and growing during the second stage.

We kept temperature and oil pressure constant during ∼30 minutes after the first burst of ϵ-Fe and tomography were collected regularly (Fig. 5). As the ratio of ϵ-Fe continued to increase, the ϵ-Fe solid grains progressively grew. These solid grains appear to be part of a second stage of the transformation.

On the contrary, the first stage platelets's thickness increased only marginally, eventually becoming corrugated. Their presence seems to inhibit the growth of second stage ϵ-Fe grains, which is likely due to a high concentration of defects close to their surface. The transformation completed around 830 K, while portions of γ-Fe phase appeared at the same time in the X-ray diffraction data.

XRD measurements (Fig. 4a) show that most of the orientations of ϵ-Fe crystals match the orientation relations predicted by Burgers path [17], confirming the observations made in previous studies by either static or dynamic compression [20, 21, 19]. A description of this path is provided in Fig. 6: a uniaxial loading compresses the atoms in the $(110)_{\mathrm{bcc}}$ plane to form regular hexagons which will form $(0001)_{\mathrm{hcp}}$ basal plane, and every other of these planes shuffles by $a_{\mathrm{bcc}}/(3\sqrt{2})$ in the $[\bar{1}10]_{\mathrm{bcc}}$ direction to produce the hcp $ABAB$ stacking. In a bcc lattice, there are six equivalent $\{110\}$ planes, and therefore six different hcp crystals (called *variants*) can be obtained with this mechanism. All expected variants are observed in Fig. 4a. Those with $(0002)_\epsilon \,||\, (1\bar{1}0)_\alpha$ and $(0002)_\epsilon \,||\, (110)_\alpha$ XRD peaks in the diffraction plane are labelled 1 and 2, respectively. $\{1\bar{1}00\}_\epsilon$ and $\{1\bar{1}01\}_\epsilon$ peaks are broadened by several degrees: this is an effect of the phase transition itself, and not pressurizing conditions, because a similar broadening is reported in Ref. [19], where the transition was induced under hydrostatic pressure. The peak labelled T is not expected by Burgers mechanism but can be obtained by $\{01\bar{1}2\}\langle 0\bar{1}11\rangle$ twinning of one Burgers variant of ϵ-Fe [38], evidencing one irreversible twinning deformation mechanism in the sample subsequent to the transformation.

The reverse $\epsilon \rightarrow \alpha$ transformation has been observed around 8 GPa and 723 K after rounding the triple point through $\alpha \rightarrow \gamma \rightarrow \epsilon$ transformations. A martensitic microstructure is also produced. The numerous α-Fe platelets formed have an extension likely limited by the size of ϵ-Fe grains (Supplementary Fig. 5).

3.3. Transformation γ to ϵ.

The $\gamma \rightarrow \epsilon$ phase transformation was induced by temperature decrease above ∼9 GPa in a γ-Fe multigrain sample. XRD measurements show that ϵ-Fe formed large grains, and a few γ-ϵ boundaries could be detected on the tomographies. However, the low density contrast between ϵ-Fe and γ-Fe (∼1.2 %) prevented a precise determination of the transformation microstructure.

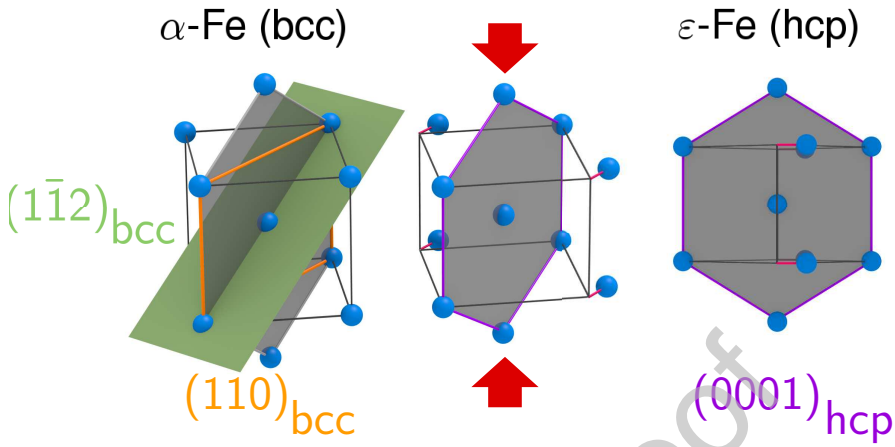

Figure 6: **Schematic of the α (bcc) $\rightarrow$ ϵ (hcp) Burgers transformation path.** It involves a compression in vertical direction (red arrows) and a shuffle of every other $(110)_{bcc}$ plane (red lines). Here, the $(110)_{bcc}$ plane transforms into the $(0001)_{hcp}$ basal plane. $(1\bar{1}2)_{bcc}$ plane, in green, is usually described as a possible *habit plane* of the transformation, as in Ref. [22] (see text).

4. Discussion

Below, we provide a quantitative analysis for the $\alpha \rightarrow \epsilon$ transformation. Observations show that it takes place in two stages: in the first stage, ϵ-Fe bursts as platelets into the α-Fe single crystals. The platelets thickness limits to $\sim$30 μm, transforming less than 20% of the sample volume. Then the transformation proceeds through a second stage, where smoother interfaces are seen to move with time and progressively increase the amount of ϵ-Fe in the sample, up to a complete transformation.

4.1. Fourier analysis of the α-ϵ microstructure

To quantitatively analyze the microstructure formed during the first stage of the $\alpha \rightarrow \epsilon$ transformation as observed in the tomographic reconstruction in Figs. 5 and 4b-e (first tomography recorded after onset of $\alpha \rightarrow \epsilon$ transformation), we calculated the Fourier transform (FT) of its density. The modulus of FT and its stereographic projections are represented in Fig. 7a and Fig. 7b, respectively. The data have been rotated in order to align the cubic axis of the α-Fe crystal lattice ([100], [010], [001]), determined with XRD, along the orthonormal vectors ($\boldsymbol{x}$, $\boldsymbol{y}$, $\boldsymbol{z}$). $\boldsymbol{z}$ is also the compression axis of the PE press. The FT has clear peaks around 12 orientations. They mark high frequencies of density variations, corresponding to the orientation of normals to interfaces between phases, mostly platelets surfaces. We thus made the hypothesis that the peaks observed in Fig. 7b correspond to habit planes for platelets formation during the first stage of the transformation.

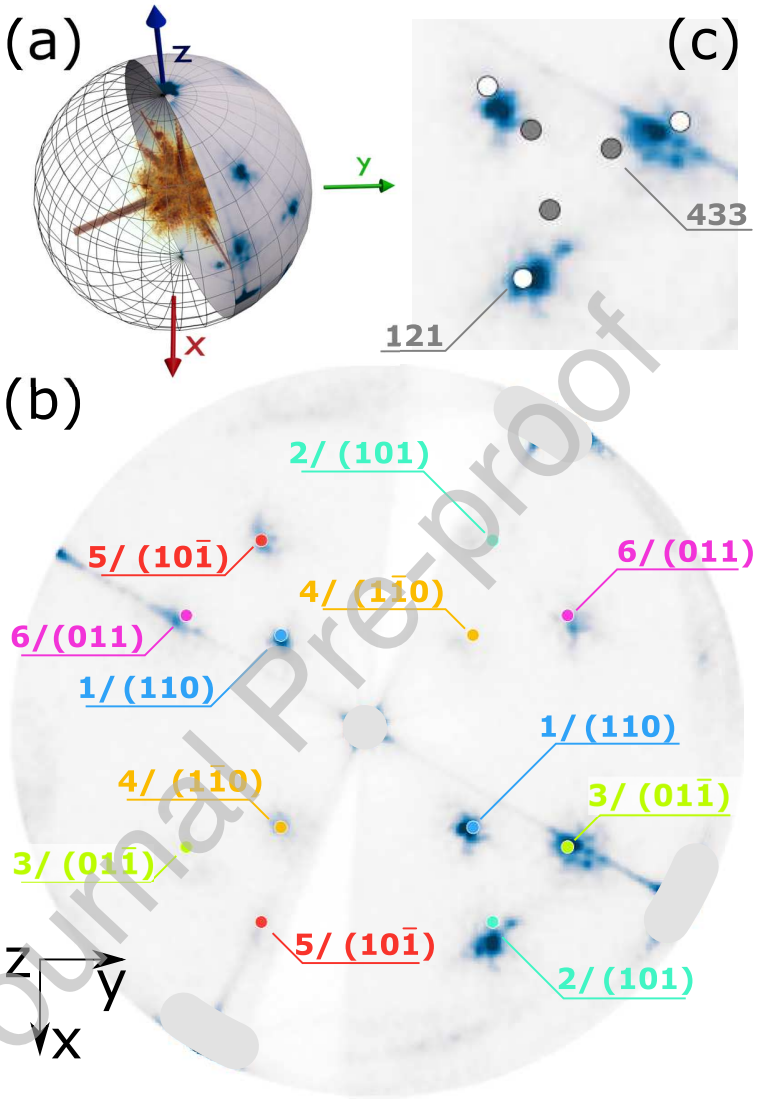

Figure 7: **Fourier analysis of the tomographic reconstruction in Fig. 4 and comparison with kinematic compatibility condition. a,** modulus of tomographic reconstruction in Fourier space and the unit sphere onto which this density is projected in **b**. **b,** stereographic projection of this modulus, represented in the α-Fe starting body-centered cubic single crystal lattice system. Z also corresponds to the compression axis of the PE press. 12 peaks correspond to high frequencies of α - ϵ interfaces normals. The normals to α - ϵ interfaces that satisfy the kinematic compatibility criterion are indicated as colored disks (see text). The index i of the transformation $\boldsymbol{U}_i$ (i=1 to 6) is indicated. The dense plane $\{110\}_{\text{bcc}}$ which is transformed into the basal plane $\{0002\}_{\text{hcp}}$ for each index i is also indicated in parenthesis. **c,** zoom on the lower-right quadrant in **b**, with a comparison between the orientations of $\{211\}_{\text{bcc}}$ and $\{433\}_{\text{bcc}}$ planes and the measured frequency peaks.

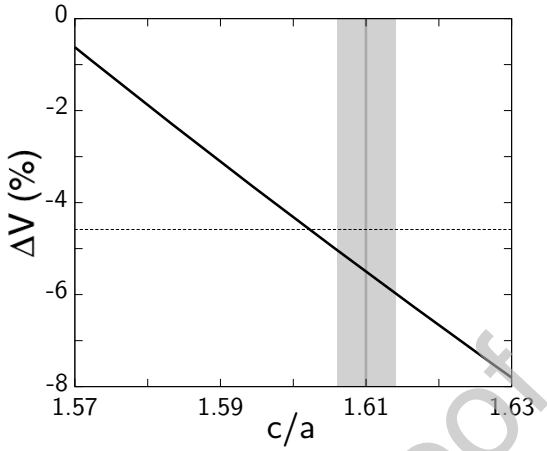

Figure 8: **α-Fe $\rightarrow$ ϵ-Fe volume discontinuity vs c/a in ϵ-Fe.** The vertical and horizontal lines and shaded zones indicate the experimental values and uncertainties around 8 GPa and 611 K [27]. The bold black line represents the trend which exactly fulfils the kinematic compatibility condition for a martensitic α-Fe $\rightarrow$ ϵ-Fe transformation.

The family of vectors $\{211\}_{\mathrm{bcc}}$ and $\{433\}_{\mathrm{bcc}}$, often mentioned as possible habit plane normals for bcc-hcp transformation [4, 25, 22, 19] (see Fig. 6), are plotted for comparison purpose (Fig. 7c). The observed peaks are close, but do not correspond exactly to these simple crystallographic directions.

4.2. Kinematic modeling of α-ϵ transformation

Below, we use a kinematic compatibility hypothesis, also called Hadamard conditions, established for displacive transformations (see [39, 40]), to calculate the interfaces for the α-Fe and ϵ-Fe lattices. We show that these conditions can be fulfilled under the current experimental conditions.

A homogeneous transformation can be described with a tensor $\boldsymbol{U}$, which transforms a vector $\boldsymbol{a}$ into a displaced one through $\boldsymbol{b} = \boldsymbol{U} \cdot \boldsymbol{a}$. The kinematic compatibility condition between two transformations $\boldsymbol{W}$ and $\boldsymbol{U}$ can be summarized as the existence of a plane such as, for any point $\boldsymbol{p}$ along this plane the displacement induced by $\boldsymbol{U}$ is equal to the one induced by $\boldsymbol{W}$ (we thus have $\boldsymbol{U} \cdot \boldsymbol{p} = \boldsymbol{W} \cdot \boldsymbol{p}$). Since the atoms in this plane belong to both phases this plane constitutes an ideal boundary (in the sense of energy minimizer), between two transformed zones.

Here, the transformation starts under high pressure, from a parent α phase that is assumed to be isotropically compressed from the ambient pressure phase at volume V_0 by $\boldsymbol{W} = \left(\frac{V}{V_0}\right)^{1/3} \boldsymbol{I}$, ($\boldsymbol{I}$ the identity matrix). The transformation α-ϵ is observed to follow the Burgers path [17, 19]. We used a deformation matrix $\boldsymbol{U}$ which describes the transformation from the

ambient pressure α phase to the high pressure ϵ phase (defined in Appendix A). Then, the relative volume discontinuity at the transition is: $\Delta V = (V_\epsilon - V_\alpha)/V_\alpha = [\det(\boldsymbol{U}) - \det(\boldsymbol{W})]/\det(\boldsymbol{W})$. We obtain that the kinematic compatibility condition (see Appendix A) can be exactly satisfied for one ΔV for each c/a (ratio between lattice parameters in hcp ϵ-Fe): ΔV vs c/a is represented in Fig. 8. Among the values compatible with the measurements close to the triple point [27], we consider a $c/a = 1.610 \pm 0.004$, corresponding to a predicted volume drop of $5.5 \pm 0.5\%$. The measured volume drop is $\sim 4.6\%$ at 611K [27], which suggests that the compatibility conditions may not be exactly fulfilled. Thus, a limited additional deformation (e.g., plasticity) to stabilize the α-ϵ interface cannot be excluded.

4.3. Comparison between predicted and experimental α-ϵ microstructures

Using kinematic compatibility model, six deformation matrices $\boldsymbol{U}_i$ corresponding to the six transformation variants for $c/a = 1.610$ have been generated. All normals $\boldsymbol{n}$ to habit planes have been calculated. Let us note that, for each of the 6 variants $\boldsymbol{U}_i$, two normals $\boldsymbol{n}$ are possible, yielding a total of 12 interfaces orientations. These orientations are plotted in Fig. 7b, one color corresponding to each variant, together with the stereographic projection of tomography Fourier transform. The calculated orientations closely match the maximum densities of interfaces in the tomographic reconstruction: this shows that ϵ-Fe platelets form in line with kinematic compatibility. The small disorientation of 4.4° with $\{211\}_{\mathrm{bcc}}$ corresponds to the minimization of lattice mismatches for the exact values of lattice parameters of both phases under relevant conditions. When the two possible normals $\boldsymbol{n}$ orientations per variant are taken into account, the volumetric fraction is almost the same for each variant. The data thus show an absence of variant selection, implying a stress close to hydrostatic pressure inside the cell assembly, despite the axial nature of the primary compression in the Paris-Edinburgh press.

Finally, the variant corresponding to each platelet in the direct space has been determined by taking the highest convolution with Hann penny-shaped window as described in Appendix B. The result, presented in Fig. 4e (and in Appendix C as full sample coverage), shows that variants of the first stage of the phase transformation are homogeneously distributed within the sample. One variant corresponding to one orientation of ϵ-Fe daughter phase, Fig. 4e is similar to what would be slices of a 3D non-destructive EBSD measurement of the microstructure during the first stage of the transformation. The grains formed during the second stage are left in black, as their orientation cannot be determined.

4.4. Evolution of the α-ϵ transformation mechanism

Our quantitative analyses of the microstructure thanks to the coupling of XRD and tomography measurements therefore show that the ϵ-Fe crystals from the first stage have an orientation predicted by Burgers path, with no variant selection, and their surfaces satisfy the kinematic compatibility criterion, which is paramount of a displacive (martensitic) transformation. The smooth interfaces of the second stage of the transformation progressively increase the amount of ϵ-Fe in the sample, up to a complete transformation. This suggests a second stage dominated by a reconstructive mechanism. In fact, transforming a large volume with a martensitic mechanism would lead to an important modification of the sample external shape, which is very costly energetically for a sample contained under pressure in a solid medium. However, XRD data show that Burgers orientation relations are also satisfied for the second stage as most of the XRD peaks satisfy these relations. ϵ-Fe thus likely grows in the second stage from a seed formed in the first stage. As a result, the final microstructure is largely influenced by the first displacive step of the transformation since the nuclei of the second phase inherit their orientation from the platelets. This transformation scenario, revealed by tomography, allows understanding why small portions of α-Fe remain largely above 13 GPa [19], the $\alpha \rightarrow \epsilon$ transformation being hindered by defects close to platelets formed in the first stage. A competitive growth of the same structure with displacive (intra-grain) and reconstructive (from grain boundaries) mechanisms has been observed in polycrystal titanium [25]. Here, the two mechanisms are observed sequentially, evidencing how the system adapts to minimize the energetic path of the transformation as it unfolds.

4.5. α-γ transformation

The microstructures induced by α (bcc) $\leftrightarrow$ γ (fcc) transformations are completely different from α (bcc) $\leftrightarrow$ ϵ (hcp) microstructures. The lack of systematic OR, together with the absence of martensitic features (platelets, wedges...) in the α-γ coexistence domain, suggest that under the experimental conditions generated here (up to 6 GPa, above $\sim$450 K, heating rate of 10^2 K/s), $\alpha \rightarrow \gamma$ transformation is reconstructive rather than displacive. This generates a smooth interface approximately following one isotherm and produces large single crystals. The absence of martensitic features in the microstructure can be partly due to the *absence* of kinematic compatibility between bcc and fcc lattices often reported in the literature [40], which we confirmed here for the conditions of the experiments. The boundary conditions, with a fixed sample shape, could also be at play. For a bcc-fcc transformation, often taught as archetypal for martensitic (displacive) transformations in steels, the evidence of a reconstructive mechanism could appear

surprising. However, it is the $\gamma \rightarrow \alpha$ observed on quenching which is clearly displacive, while $\alpha \rightarrow \gamma$ transition is often described as reconstructive, a combined effect of temperature and alloying [4].

5. Conclusion

This work establishes the importance of characterizing the transient state in allotropic transformation to identify the mechanisms. In particular, we show that pressure-induced α-Fe $\rightarrow$ ϵ-Fe presents two successive different steps which both affect the final microstructure. Such monitoring can be used to tailor materials with outstanding mechanical or thermal properties. To that purpose, in-situ X-Ray tomography coupled with X-Ray diffraction allow for a quantitative microstructure analysis and are demonstrated to be ideal and non-destructive tools, which should spread with the advent of new generation synchrotrons and data analysis techniques.

Appendix A. Compatibility conditions

We are seeking the existence of compatible interfaces between ϵ-Fe (hcp) and α-Fe (bcc), the two phases being deformed by (respectively) a transformation $\boldsymbol{U}$ and $\boldsymbol{W}$ (transformations defined in large strain formalism). The kinematics of the bcc to hcp phase transition such as described by Burgers [17] and Mao et al. [10] is defined by the following transformation [41]:

$$\boldsymbol{U} = \begin{bmatrix} \frac{3}{4\sqrt{2}} + \frac{1}{4}\sqrt{\frac{3}{2}}\frac{c}{a} & -\frac{3}{4\sqrt{2}} + \frac{1}{4}\sqrt{\frac{3}{2}}\frac{c}{a} & 0 \\ -\frac{3}{4\sqrt{2}} + \frac{1}{4}\sqrt{\frac{3}{2}}\frac{c}{a} & \frac{3}{4\sqrt{2}} + \frac{1}{4}\sqrt{\frac{3}{2}}\frac{c}{a} & 0 \\ 0 & 0 & \frac{\sqrt{3}}{2} \end{bmatrix} k^{1/3} \tag{A.1}$$

which depends on the ratio c/a. The factor k is such as the volume change induced by the transformation $\boldsymbol{U}$ corresponds to the experimental value (in the present case, the forward transformation at 611K and 13.8 GPa described in [27]). We assume the parent phase before transformation to be isotropically compressed by $\boldsymbol{W} = (V/V0)^{1/3}\,\boldsymbol{I}$. The compatibility condition between two zones deformed by $\boldsymbol{U}$ and $\boldsymbol{W}$ is equivalent to find two vectors $\boldsymbol{n}$ and $\boldsymbol{a}$ such as $\boldsymbol{U} - \boldsymbol{W} = \boldsymbol{a} \otimes \boldsymbol{n}$, with $\boldsymbol{n}$ the normal of the compatible plane and $\otimes$ the tensor product ($\boldsymbol{a} \otimes \boldsymbol{b} = a_i b_j$). To find the normal $\boldsymbol{n}$, we express the relative transformation between the parent and the daughter phase as $\boldsymbol{G} = \boldsymbol{U} \cdot \boldsymbol{W}^{-1}$ and its Cauchy-Green tensor $\boldsymbol{C} = \boldsymbol{G}^{\mathrm{T}} \cdot \boldsymbol{G}$. An invariant plane exists (see [39, 40]) if the eigen values of $\boldsymbol{C}$ are such as $\lambda_1 < 1$, $\lambda_2 = 1$, $\lambda_3 > 1$. The normal $\boldsymbol{n}$ of this plane is proportional to:

$$\hat{\boldsymbol{n}} = \frac{\sqrt{\lambda_3} - \sqrt{\lambda_1}}{\sqrt{\lambda_3 - \lambda_1}} \left(-\sqrt{1 - \lambda_1}\boldsymbol{e}_1 \pm \sqrt{\lambda_3 - 1}\boldsymbol{e}_3 \right) , \tag{A.2}$$

with $\boldsymbol{e}_1$ and $\boldsymbol{e}_3$ the eigen vectors of the eigen values λ_1 and λ_3, respectively.

For values of c/a ranging between 1.57 and 1.63, we found only one value of V fulfilling the requested constraint, plotted as a volume variation in Fig. 8. To consider all possible variants of the α-Fe $\rightarrow$ ϵ-Fe transformations, six transformation matrices $\boldsymbol{U}_i$ have been generated from $\boldsymbol{U}$, corresponding to the six possible choices of $\{110\}_{\text{bcc}}$ dense planes to produce the basal $\{0002\}_{\text{hcp}}$ plane (see Fig. 6) and rotations of the bcc rotations point group.

Appendix B. Volume indexation

We define the index i of a point $\boldsymbol{r}$ in the sample as the index of the normal $\boldsymbol{n}_i$ that best describes the local orientation of a variation of density. To do so, we create 12 penny-shaped Hann window functions $h(\boldsymbol{r})$ with orientation $\boldsymbol{n}_i$, defined by

$$h(\boldsymbol{r}) = \frac{1}{2}\left\{1 + \cos\left[\pi \min(1, |\boldsymbol{S}\cdot\boldsymbol{r}|)\right]\right\} \tag{B.1}$$

with $\boldsymbol{S} = \boldsymbol{I} + (s-1)\boldsymbol{n}_i \otimes \boldsymbol{n}_i$ a transformation matrix expanding the space in the direction of $\boldsymbol{n}_i$ by a factor s and $\otimes$ the tensor product. We then perform the convolution (with a FFT technique) of the tomography density function with all functions h_i and select the index i of highest value for the convolution product. As a last operation, we perform the same convolution but with isotropic Hann function ($s = 1$), and compare the convolution product with the previous highest value. When the two results differ by less than a few percent, there is no preferred orientation of the density variations, and no index is proposed (plotted as black zone in Fig. 4ce). When one index i yields a high convolution of h_i with density distribution at $\boldsymbol{r}$, this indicates that $\boldsymbol{r}$ is close to an interface with normal $\boldsymbol{n}_i$ and the point is represented in the color associated to i. In all presented results, $s = 10$ and the penny-shaped function has a diameter of 87.3μm for a thickness of 8.73μm.

Appendix C. Section planes for α-Fe $\rightarrow$ ϵ-Fe transformation

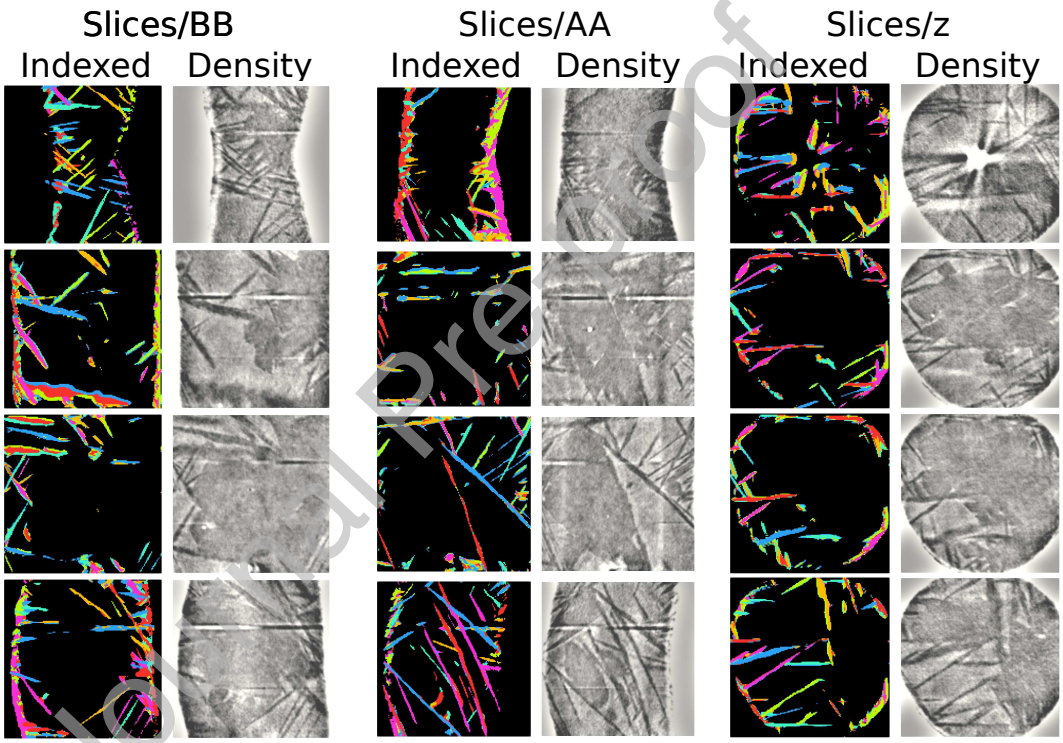

Figure C.9: **Section planes from a reconstructed volume collected on the α-Fe $\rightarrow$ ϵ-Fe transformation represented in Fig. 4.** The colouring of platelets corresponds to the variants identified from their surface orientations, with the same colour scale as in Fig. 4. The slices have been made every 52 microns.

Table C.1: Volume V (in cm^3/mol) measured in bcc α-Fe ($V = a^3/2$), fcc γ-Fe ($V = a^3/4$) and hcp ϵ-Fe ($V = a^2c\sqrt{3}/4$), the associated pressure (using [35] for ϵ-Fe and [36] for α-Fe and γ-Fe), and lattice parameters a anc c for ϵ-Fe. The data are presented in the order they have been recorded.

Nb.	T (K)	P_{BN} (GPa)	V_{bcc}	P_{bcc} (GPa)	V_{fcc}	P_{fcc} (GPa)	V_{hcp}	c_{hcp} Å	a_{hcp} Å	P_{hcp} (GPa)
Fe2	947				6.909	5.214				
	942		7.045	5.091	6.929	4.742				
	917		7.029	5.378						
	895		7.045	4.798						
Fe7	413	5.192	6.897	5.670						
	641	5.191	6.979	4.959						
	758		7.029	4.367						
	850		7.045	4.513						
	900				6.905	4.799				
Fe10	296	-0.003	7.103	-0.315						
	363	0.335	7.112	-0.117						
	430	1.175								
	503	3.032	7.045	2.338						
	546	3.753	7.029	3.020						
	645	4.530	7.029	3.652						
	919	4.825	7.112	3.203	6.929	4.502				
	917	4.820	7.080	4.030	6.950	4.036				
	973	4.943			6.950	4.643				
	927				6.929	4.588				
	884		7.062	4.299	6.929	4.127				
	909		7.062	4.449	6.929	4.387				
	876	4.940	7.062	4.249	6.888	4.918				
	296	4.013	6.922	4.177						
Fe11	598	2.360	7.096	1.680						
	747	2.448	7.127	1.809						
	792		7.130	2.000						
	1010		7.233	0.767	7.161	1.126				
	1028		7.215	1.290						
	1048				7.097	2.645				
	1060				7.097	2.777				
	1016		7.199	1.617	7.071	2.749				
	1019		7.199	1.634	7.034	3.477				

Table C.2: continued.

Nb.	T (K)	P_{BN} (GPa)	V_{bcc}	P_{bcc} (GPa)	V_{fcc}	P_{fcc} (GPa)	V_{hcp}	c_{hcp} Å	a_{hcp} Å	P_{hcp} (GPa)
Fe12	300	-0.062	7.112	-0.496						
	647	5.120	7.012	4.125						
	830		7.012	5.305						
	880		7.062	4.269	6.867	5.416				
	1093	5.791			6.909	6.777				
	1043	7.121			6.827	8.071				
	1068	8.162			6.827	8.333				
	1048	9.653			6.726	10.580				
	949				6.707	10.051	6.619	4.055	2.502	8.293
	890	9.344			6.726	8.928	6.598	4.054	2.499	8.404
	810				6.726	8.102	6.594	4.045	2.501	7.904
Fe13	300	-0.058	7.130	-0.898						
	741		7.012	4.731						
	900		7.029	5.267	6.888	5.165				
	961				6.929	4.952				
	1005		7.045	5.491	6.888	6.294				
	1063	5.874			6.909	6.457				
	1050	8.644			6.787	9.089				
	1036	9.544			6.747	9.936				
	922				6.726	9.263				
	869				6.687	9.763				
	772				6.726	7.701	6.611	4.070	2.496	7.123
	794				6.687	8.986	6.605	4.061	2.498	7.455
	816				6.687	9.215	6.633	4.048	2.507	6.877
	842				6.726	8.436	6.638	4.056	2.506	6.930
	895				6.726	8.987				
	851				6.726	8.528				
	820				6.707	8.714	6.631	4.071	2.500	6.960
	794				6.687	8.986	6.631	4.071	2.500	6.754
	723	8.883	6.865	8.805	6.707	7.706	6.627	4.040	2.508	6.314
	679		6.865	8.488	6.747	6.204	6.594	4.045	2.501	6.896
	617		6.865	8.045	6.687	7.159	6.561	4.049	2.493	7.351
	560		6.848	8.154	6.668	7.099	6.542	4.048	2.490	7.478
	503	8.407	6.832	8.215	6.668	6.506	6.550	4.033	2.496	6.837

Table C.3: continued.

Nb.	T (K)	P_{BN} (GPa)	V_{bcc}	P_{bcc} (GPa)	V_{fcc}	P_{fcc} (GPa)	V_{hcp}	c_{hcp} Å	a_{hcp} Å	P_{hcp} (GPa)
Fe14	300	-0.06	7.130	-0.898						
	426	3.910	6.995	3.122						
	422	5.384	6.929	4.843						
	420	6.064	6.897	5.717						
	417	6.847	6.897	5.701						
	411	7.601	6.848	7.070						
	471	9.143	6.832	7.981						
	471	9.583	6.816	8.463						
	468	9.716	6.784	9.426						
	509	9.810	6.800	9.234						
	591		6.832	8.864						
	722		6.832	9.827						
	800	10.24	6.848	9.895	6.629	10.653	6.580	4.051	2.496	8.198
	757	9.990	6.832	10.089	6.648	9.674	6.556	4.041	2.495	8.582
	829		6.848	10.105	6.668	9.872	6.580	4.051	2.496	8.423
	889				6.668	10.491	6.608	4.038	2.505	8.126
	962				6.668	11.249				

References

[1] L. J. Swartzendruber, The fe (iron) system, Bull. Alloy Phase Diagrams 3 (1982) 161.

[2] I. Leonov, Electronic correlations determine the phase stability of iron up to the melting temperature, Sci. Rep. 4 (2014) 5585.

[3] J. Neuhaus, M. Leitner, K. Nicolaus, W. Petry, B. Hennion, A. Hiess, Role of vibrational entropy in the stabilization of the high-temperature phases of iron, Phys. Rev. B 89 (18) (2014) 184302. doi:10.1103/PhysRevB.89.184302.

[4] Z. Nishiyama, Martensitic transformations, Academic, New York, 1978.

[5] R. Zerwekh, C. Wayman, On nature of alpha -gamma transformation in iron - a study of whiskers, Acta Metall. 13 (2) (1965) 99–107. doi:10.1016/0001-6160(65)90159-8.

[6] A. M. Balagurov, I. A. Bobrikov, I. S. Golovin, Anomalous behavior of an alpha - gamma phase transition in iron: Results of in situ neutron diffraction experiment, JETP Lett. 107 (9) (2018) 558–563. doi:10.1134/S0021364018090060.

[7] N. Bruzy, M. Coret, B. Huneau, L. Stainier, C. Denoual, M. Mondon, G. Kermouche, Real time imaging of strain fields induced by the ferrite-to-austenite transformation in high purity iron, Materials Today Communications 24 (2020) 101028. doi:https://doi.org/10.1016/j.mtcomm.2020.101028.

[8] D. Bancroft, E. L. Peterson, S. Minshall, Polymorphism of iron at high pressure, J. Appl. Phys. 27 (1956) 291.

[9] J. Jamieson, A. Lawson, X-ray diffraction studies in 100 kilobar pressure range, J. Appl. Phys. 33 (3) (1962) 776–780. doi:10.1063/1.1777167.

[10] H.-K. Mao, W. Bassett, T. Takahashi, Effect of pressure on crystal structure and lattice parameters of iron up to 300 kbar, J. Appl. Phys. 38 (1) (1967) 272–276.

[11] O. Mathon, F. Baudelet, J.-P. Itié, A. Polian, M. D'Astuto, J.-C. Chervin, S. Pascarelli, Dynamics of the magnetic and structural alpha-epsilon phase transition in iron, Phys. Rev. Lett. 93 (2004) 255503.

[12] L. Stixrude, R. E. Cohen, D. Singh, Iron at high-pressure - linearized-augmented-plane-wave computations in the generalized-gradient approximation, Phys. Rev. B 50 (9) (1994) 6442–6445. doi:10.1103/PhysRevB.50.6442.

[13] B. Dupé, B. Amadon, Y.-P. Pellegrini, C. Denoual, Mechanism for the alpha - epsilon phase transition in iron, Phys. Rev. B 87 (2) (JAN 7 2013). doi:10.1103/PhysRevB.87.024103.

[14] S. Tateno, K. Hirose, Y. Ohish, Y. Tatsumi, The structure of iron in the earth's inner core, Science 330 (2010) 359–361.

[15] P. Giles, M. Longenbach, A. Marder, High-pressure α-ϵ martensitic transformation in iron, J. Appl. Phys. 42 (11) (1971) 4290–4295. doi:10.1063/1.1659768.

[16] R. Boehler, N. V. Bargen, A. Chopelas, Melting, thermal expansion, and phase transitions of iron at high pressure, J. Geophys. Res. 95 (1990) 21731–21736.

[17] W. Burgers, On the process of transition of the cubic-body-centered modification into the hexagonal-close-packed modification of zirconium, Physica 1 (7–12) (1934) 561–586. doi:http://dx.doi.org/10.1016/S0031-8914(34)80244-3.

[18] S. Merkel, H.-P. Liermann, L. Miyagi, H.-R. Wenk, In situ radial x-ray diffraction study of texture and stress during phase transformations in bcc-, fcc- and hcp-iron up to 36 gpa and 1000 k, Acta Mater. 61 (14) (2013) 5144 – 5151. doi:http://dx.doi.org/10.1016/j.actamat.2013.04.068.

[19] A. Dewaele, C. Denoual, S. Anzellini, F. Occelli, M. Mezouar, P. Cordier, S. Merkel, M. Vron, E. Rausch, Mechanism of the $\alpha - \epsilon$ phase transformation in iron, Phys. Rev. B 91 (2015) 174105.

[20] D. H. Kalantar, J. F. Belak, G. W. Collins, J. D. Colvin, H. M. Davies, J. H. Eggert, T. C. Germann, J. Hawreliak, B. L. Holian, K. Kadau, P. S. Lomdahl, H. E. Lorenzana, M. A. Meyers, K. Rosolankova, M. S. Schneider, J. Sheppard, J. S. Stölken, J. S. Wark, Direct observation of the alpha-epsilon transition in shock-compressed iron via nanosecond x-ray diffraction, Phys. Rev. Lett. 95 (2005) 075502.

[21] J. Hawreliak, J. D. Colvin, J. H. Eggert, D. H. Kalantar, H. E. Lorenzana, J. S. Stolken, H. M. Davies, T. C. Germann, B. L. Holian, K. Kadau, P. S. Lomdahl, Analysis of the x-ray diffraction signal for

the alpha-epsilon transition in shock-compressed iron: Simulation and experiment, Phys. Rev. B 74 (2006) 184107.

[22] S. J. Wang, M. L. Sui, Y. T. Chen, Q. H. Lu, E. Ma, X. Y. Pei, Q. Z. Li, H. B. Hu, Microstructural fingerprints of phase transitions in shock-loaded iron, Sci. Rep. 3 (JAN 18 2013). doi:10.1038/srep01086.

[23] S. Ackermann, S. Martin, M. Schwarz, C. Schimpf, D. Kulawinski, C. Lathe, S. Henkel, D. D. Rafaja, H. Biermann, A. Weidner, Investigation of phase transformations in high-alloy austenitic trip steel under high pressure (up to 18 GPa) by in situ synchrotron x-ray diffraction and scanning electron microscopy, Metall. Mat. Trans A 47A (1) (2016) 95–111. doi:10.1007/s11661-015-3082-2.

[24] A. Vattré, C. Denoual, Polymorphism of iron at high pressure: A 3d phase-field model for displacive transitions with finite elastoplastic deformations, J. Mech. Phys. Solids 92 (2016) 1–27. doi:10.1016/j.jmps.2016.01.016i.

[25] G. Seward, S. Celotto, D. Prior, J. Wheeler, R. Pond, In situ SEM-EBSD observations of the hcp to bcc phase transformation in commercially pure titanium, Acta Mat. 52 (4) (2004) 821–832. doi:10.1016/j.actamat.2003.10.049.

[26] N. Vigano, A. T. , S. Hallais, A. Dimanov, M. Bornert, K. J. Batenburg, W. Ludwig, Three-dimensional full-field x-ray orientation microscopy, Sci. Rep. 6 (2016) 20618. doi:10.1038/srep20618.

[27] A. Dewaele, V. Svitlyk, F. Bottin, J. Bouchet, J. Jacobs, Iron under conditions close to the alpha-gamma-is an element of triple point, Appl. Phys. Lett. 112 (20) (MAY 14 2018). doi:10.1063/1.5030192.

[28] J. M. Besson, G. Hamel, T. Grima, R. J. Nelmes, J. S. Loveday, S. Hull, D. Häusermann, A large volume pressure cell for high temperatures, High Press. Res. 8 (5-6) (1992) 625–630.

[29] S. Klotz, G. Hamel, J. Frelat, A new type of compact large-capacity press for neutron and x-ray scattering, High Press. Res. 24 (1) (2004) 219–223. doi:10.1080/08957950410001661963.

[30] E. Boulard, A. King, N. Guignot, J. Deslandes, Y. Le Godec, A. Clark, G. Morard, J.-P. Itié, High-speed tomography under extreme conditions at the psiche beamline of the soleil synchrotron, J. Synchrotron Rad. 25 (3) (2018) 818–825. doi:https://doi.org/10.1107/S1600577518004861.

[31] J. Philippe, Y. Le Godec, M. Mezouar, M. Berg, G. Bromiley, F. Bergame, J. P. Perrillat, M. Alvarez-Murga, M. Morand, R. Atwood, A. King, S. Régnier, Rotating tomography parisedinburgh cell: a novel portable press for micro-tomographic 4-d imaging at extreme pressure/temperature/stress conditions, High Press. Res. 36 (4) (2016) 512–532. doi:10.1080/08957959.2016.1221951.

[32] A. King, N. Guignot, P. Zerbino, E. Boulard, K. Desjardins, M. Bordessoule, N. Leclerq, S. Le, G. Renaud, M. Cerato, M. Bornert, N. Lenoir, S. Delzon, J.-P. Perrillat, Y. Legodec, J.-P. Itié, Tomography and imaging at the psiche beam line of the soleil synchrotron, Rev. Sci. Instrum. 87 (9) (2016) 093704. doi:10.1063/1.4961365.

[33] A. Mirone, E. Brun, E. Gouillart, P. Tafforeau, J. Kieffer, The PyHST2 hybrid distributed code for high speed tomographic reconstruction with iterative reconstruction and a priori knowledge capabilities, Nucl. Instrum. Meth. B 324 (2014) 41–48.

[34] Y. Wang, T. Uchida, R. V. Dreele, M. L. Rivers, A new technique for angle-dispersive powder diffraction using an energy-dispersive setup and synchrotron radiation research papers, J. Appl. Cryst. 37 (2004) 947–956. doi:10.1107/S0021889804022502.

[35] A. Dewaele, P. Loubeyre, F. Occelli, M. Mezouar, P. I. Dorogokupets, M. Torrent, Quasihydrostatic equation of state of iron above 2 mbar, Phys. Rev. Lett. 97 (2006) 215504–215507.

[36] T. Komabayashi, Y. Fei, Internally consistent thermodynamic database for iron to the Earth's core conditions, J. Geophys. Res. 115 (2010) B03202. doi:10.1029/2009JB006442.

[37] K. Fuchizaki, T. Nakamichi, H. Saitoh, Y. Katayama, Equation of state of hexagonal boron nitride, Solid State Commun. 148 (9-10) (2008) 390–394. doi:10.1016/j.ssc.2008.09.031.

[38] D. Sun, M. Ponga, K. Bhattacharya, M. Ortiz, Proliferation of twinning in hexagonal close-packed metals: Application to magnesium, J. Mech. Phys. Solids 112 (2018) 368–384. doi:10.1016/j.jmps.2017.12.009.

[39] J. M. Ball, R. D. James, Fine phase mixtures as minimizers of energy, Archive for Rational Mechanics and Analysis 100 (1) (1987) 13–52. doi:10.1007/BF00281246.

[40] K. Bhattacharya, Microstructure of Martensite: why it forms and how it gives rise to the shape-memory effect, Oxford University Press, 2003.

[41] A. Lew, K. Caspersen, E. Carter, M. Ortiz, Quantum mechanics based multiscale modeling of stress-induced phase transformations in iron, J. Mech. Phys. Solids 54 (2006) 1276–1303.

Acknowledgements

EB acknowledges financial support from CEA-DIF during years 2017-2018. The authors acknowledge synchrotron SOLEIL for the provision of beamtime under proposal 20171509. We thank J.P. Itié for sharing beamtime. We thank M. Mezouar for lending us sintered diamond anvils for PE press.

Declaration of competing interest

The authors declare no competing interests.

Declaration of interests

☑ The authors declare that they have no known competing financial interests or personal relationships that could have appeared to influence the work reported in this paper.

☐The authors declare the following financial interests/personal relationships which may be considered as potential competing interests: